NJC

Accepted Manuscript

This is an *Accepted Manuscript*, which has been through the Royal Society of Chemistry peer review process and has been accepted for publication.

Accepted Manuscripts are published online shortly after acceptance, before technical editing, formatting and proof reading. Using this free service, authors can make their results available to the community, in citable form, before we publish the edited article. We will replace this *Accepted Manuscript* with the edited and formatted *Advance Article* as soon as it is available.

You can find more information about *Accepted Manuscripts* in the Information for Authors.

Please note that technical editing may introduce minor changes to the text and/or graphics, which may alter content. The journal's standard Terms & Conditions and the Ethical guidelines still apply. In no event shall the Royal Society of Chemistry be held responsible for any errors or omissions in this *Accepted Manuscript* or any consequences arising from the use of any information it contains.

ROYAL SOCIETY OF CHEMISTRY

www.rsc.org/njc

Reduced Graphene Oxide-CdS Nanocomposites with Enhanced Visible-light Photoactivity Synthesized Using Ionic-liquid Precursors

Nan Jiang[a, †], Zhiliang Xiu[a, d, †], Zheng Xie*[, b], Hongyun Li[c]，Gang Zhao[a]，Wenpeng Wang[a]，Yongzhong Wu*[, a], Xiaopeng Hao[a]

[a]State Key Laboratory of Crystal Materials, Shandong University, Jinan 250100, P.R. China.

[b]Technical Institute of Physics and Chemistry Chinese Academy of Sciences, Beijing 100190, P. R. China

[c]High School Affiliated to Shandong University, Shandong University, Jinan 250100, P. R. China

[d]Department of Materials Science and Engineering, Shandong Polytechnic University, Jinan 250353, P. R. China.

[†]These two authors contribute equally.

ABSTRACT

A series of reduced graphene oxide and CdS nanocomposites (RGO/CdS) with different weight ratios of RGO have been synthesized by a facile microwave-assisted solvothermal method, in which the room temperature ionic-liquid 1-butyl-3-methylimidazolium thiocyanate ([BMIM]•SCN) served as sulfur source as well as stabilizing agent. RGO sheets were uniformly

decorated by CdS nanospheres in the as-prepared samples. Only the aggregates of CdS particles over 100 nm were obtained, when graphene oxides were not employed. The existence of RGO could effectively enhance the photocatalytic activity for the degradation of rhodamine B (RhB) under visible light irradiation and the RGO/CdS-10% sample possessed the highest activity and excellent stability. The improved photocatalytic efficiency of RGO/CdS nanocomposites could be attributed to the enhanced adsorbability of RhB molecules, a broadened light response range in the visible spectrum and improved separation efficiency of electron-hole pairs, all of which are resulted from the introduction of RGO. It is hoped that this facile and efficient synthesis route can promote the exploration and utilization of graphene-based semiconductor nanocomposites as visible-light photocatalysts.

Keywords: room temperature ionic-liquid precursors, CdS nanospheres, reduced graphene oxide, nanocomposites, photocatalysts

1. Introduction

With mild reaction conditions, high efficiency and the inexhaustible solar energy source, photocatalysis technology has been considered as an ideal “green” approach to solve environmental pollution and energy shortages. Extensive research on high efficiency photocatalytic materials has been carried out. As well known, ultraviolet (UV) light contributes only about 4% of solar radiation energy, while visible light accounts for about 43%, so most of the studies have been focused on the development of visible-light responsive photocatalysts[1-3].

In the last decades, the binary Ⅱ - Ⅵ chalcogenide nanomaterials, especially CdS

nanoparticles, have become the material of high interest for photocatalytic research. CdS has a narrow band gap (2.42 eV) that responds to visible light[4]. However, there are several issues that still limit the photocatalytic activity of CdS, such as the low separation efficiency of electron-hole pairs, severe aggregation to large particle size and serious photocorrosion[5, 6]. In order to solve these problems, several approaches have been tried, including the synthesis of CdS quantum dots[7, 8], deposition of noble metals[9, 10] and preparation of heterogeneous semiconductors with other components[11-14].

Recently, graphene based materials have been explored to improve the efficiency of photocatalysis due to the excellent electrical characteristics of graphene. Specifically, composites of graphene with CdS have been paid close attention with the goal of combining these two promising components. Liu et al[14] produced a graphene-CdS composite to improve the photocatalytic reduction of Cr(Ⅵ); Xu et al[15, 16] synthesized graphene-CdS nanocomposites with enhanced efficiency for photocatalytic selective organic transformation by different methods. These reports focused attention on the enhancement of photocatalytic activity. The study of the influence of graphene on the morphology and other properties of the nanocomposite has been less concerned and remains to be evaluated.

In the previous reports, hydrazine hydrate or other reductants were always used to convert lamellar solid graphene oxides (GO) into graphene through complex processes. However, most of the reductants have strong reducibility which may cause extra damage. In this work, we prepared a composite of reduced graphene oxide (RGO) sheets and CdS nanoparticles (RGO/CdS) by means of a microwave-assisted process using room temperature ionic-liquids (ILs) as precursor.

Compared with organic solvents, ILs own unique properties such as very low vapor pressure, wide liquid temperature range, good ionic conductivity, good thermal stability, good dissolving ability, excellent microwave absorbing ability[17]. To date, a variety of inorganic nanomaterials such as metal oxides (Fe_2O_3 hollow microspheres and nanorods, CuO peachstone-like architectures, etc.), metal salts (AgBr, AgCl microspheres, $SmVO_4$ nanosheets, $MnCO_3$ hollow microspheres, etc.) and metal chalcogenides (MoS_2 microspheres, ZnS nanoparticles, In_2S_3 microspheres, various Bi_2S_3 nanostructures, Bi_2Se_3nanodiscs, etc.)[18-27], have been fabricated using suitable IL-related reaction routes. In these previous reports, ILs acted not only as solvents but also as soft templates or capping agents even reactants for the fabrication of nanostructures.

In this article, the room temperature ionic-liquid 1-butyl-3-methylimidazolium thiocyanate ([BMIM]•SCN) were used as the sulfur source as well as stabilizing agent and cadmium thiocyanate ($Cd(SCN)_2$) used as the cadmium source. A series of RGO /CdS nanocomposites with different RGO weight ratios were synthesized by a facile microwave-assisted solvothermal method. The as-prepared RGO/CdS nanocomposite displayed high efficiency in the photodegradation of rhodamine B (RhB) as a visible-light-driven photocatalyst. Moreover, the influences of RGO on the properties of the nanocomposites were systematically investigated, and a tentative mechanism for the photocatalytic reaction in this system is proposed.

2. Experimental Section

2.1 Preparation of the RGO/CdS Nanocomposites

Materials. Cadmium nitrate ($Cd(NO_3)_2 \cdot 4H_2O$), potassium thiocyanate (KSCN), absolute ethanol, methanol, ethylene glycol (EG) and rhodamine B (RhB) were analytical grade. The room

temperature ionic liquid, 1-butyl-3-methylimidazolium thiocyanate ([BMIM]•SCN) was purchased from Shanghai Chengjie Chemical Co. Ltd. All materials were used without further purification.

Graphene oxide (GO) was obtained from the oxidation of graphite powder according to the modified Hummers' method[28]. Cadmium thiocyanate ($Cd(SCN)_2$) was obtained by the coprecipitation of $Cd(NO_3)_2$•$4H_2O$ in methanol with KSCN. Then the precipitate was filtered and evaporated to form powders at room temperature. A typical synthesis of RGO/CdS nanocomposites involved the following process. 0.3426 g $Cd(SCN)_2$ and 1.5 mmol of [BMIM]•SCN were dissolved in 10 mL of ethylene glycol. Concomitantly, the as-prepared GO with the desired weight ratio was dispersed in 10 mL of ethylene glycol by ultrasound for 10 min. After that, the two solutions were mixed under constant stirring for 10 min, and then transferred into a microwave reactor with a capacity of 80 mL. The reactor was heated and maintained at 180 ℃ for 20 min using a microwave system (MDS-8, Shanghai Xinyi Co, Ltd) and then cooled to room temperature naturally. The product was collected by centrifugation, washed several times with deionized water and absolute ethanol, and then dried in vacuum at 80 ℃ for 10 h. Pure CdS particles were prepared following the same procedure of the RGO/CdS nanocomposites without addition of GO.

2.2 Characterization

Powder X-ray diffraction (XRD) patterns were recorded on a Bruker D8-Avance X-ray powder diffractometer with a Cu-Kα radiation tube over the range of $20^\circ \leq 2\theta \leq 70^\circ$ (λ=0.154056 nm, the accelerating voltage and the applied current were 40 kV and 35 mA, respectively). Scanning electron microscopy (SEM) images were collected using a Hitachi S-4800 microscope equipped

with an energy-dispersive X-ray analyzer (EDS, Horiba EMAX Energy EX-350). The transmission electron microscope (TEM) analyses were carried out with a JEM-100CX field emission electron microscope. UV-vis diffuse reflectance spectra (DRS) were obtained with a Shimadzu UV2550 recording spectrophotometer equipped with an integrating sphere from 200 to 800 nm. $BaSO_4$ was used as a reference. Nitrogen adsorption-desorption measurements were conducted at 423 K on a Micromeritics ASAP-2020 analyzer. The multipoint BET surface area was calculated from the adsorption data. Raman spectra were obtained by the Lab RAM HR system of Horiba JobinYvon at room temperature using a 532 nm solid state laser as excitation source. Fourier transform infrared spectroscopy (FTIR) measurements were carried out using a Nicolet FTIR760 infrared spectrometer. X-ray photoelectron spectroscopy (XPS, Thermo ESCALAB 250) was performed using monochromated Al Ka radiation (1486.8 eV).

2.3 Photocatalytic Activity Test

The photocatalytic activity of the samples was evaluated by monitoring the degradation of RhB under light from a 50 W Xe lamp (PLS-SXE300C) equipped with cutoff filters to provide visible light ($\lambda \geq 420$ nm). Typically, a mounted 20 mg photocatalyst was suspended in a 40 mL RhB solution (1×10^{-5} mol•L^{-1}) under constant stirring. Prior to irradiation, the suspension was magnetically stirred in the dark for 30 min to ensure adsorption equilibrium of the dyes on the catalyst surface. After that, the lamp was turned on and the distance between the suspension and light source was fixed at 10 cm. At specific time intervals, 4 mL aliquots were sampled and centrifuged to remove the catalyst. The degraded solutions were examined spectrophotometrically by measuring the absorbance at 553 nm on a UV-vis spectrometer (Shimadzu UV-2500). The

degree of degradation was expressed by C/C_0, which is the ratio of the temporal RhB concentration to the initial RhB concentration after absorption equilibrium. The normalized temporal concentration changes (C/C_0) of RhB were found to be proportional to the normalized maximum absorbance (A/A_0).

2.4 Electrochemical Activity Test

Electrochemical test systems were composed of a CHI660B workstation with a three-electrode configuration using the prepared samples as the working electrodes, a Pt wire as the counter electrode, and Ag/AgCl as the reference electrode. A 50 W Xe lamp with a cutoff filter ($\lambda \geq 420$ nm) served as the visible-light source and 1M Na_2SO_4 aqueous solution was used as the electrolyte. Working electrodes were prepared as follows: 10 mg RGO/CdS nanocomposites were dispersed in absolute ethanol, and then the suspension was directly deposited onto an indium-tin oxide (ITO) glass plate and then dried at 80℃ in an vacuum oven. Electrochemical impedance measurements (EIS) were performed over the frequency range from 0.05 to 100 kHz at open-circuit potential, and the amplitude of the applied sinusoidal voltage was 10 mV.

3 Results and Discussion

3.1 Structure and Morphology of the RGO/CdS Nanocomposites

Fig. 1 shows the XRD patterns of GO, CdS and the RGO/CdS with different RGO weight ratios. In Fig. 1a, the sharp (002) peak of GO is located at $2\theta=10.69°$, corresponding to an interlayer distance of 0.827 nm. This indicates a well-ordered, lamellar GO structure, as a result of the presence of intercalated H_2O molecules and various oxygen-containing functional groups[29, 30]. It is obvious that the pure CdS and the RGO/CdS nanocomposites possess similar XRD pattern as

shown in Fig. 1b-f. The peaks at 2θ values of 24.8 °, 26.5 °, 28.2 °, 43.7 °, 47.8 °and 51.8 ° can be ascribed to the (100), (002), (101), (110), (103) and (112) crystal planes of hexagonal CdS (JCPDS 41-1049), respectively. The broadened peaks indicate that the crystallite size of the CdS nanoparticles is relatively small. While no typical diffraction peaks for the carbon species are observed in the composites, because the relatively low diffraction intensity of the expected RGO peak at 26° is most likely shielded by the main hexagonal CdS peak at 26.5° [6]. Clearly, the RGO/CdS composite is of high crystallinity just like the pure CdS sample. It is well known that the CdS particles are apt to aggregate together during the nucleation process and microwave radiation provides a quite rapid heating rate, which are not ideal conditions for the crystallization of CdS. However, RGO offers a better platform for the nucleation of the CdS nanoparticles during the microwave heating process[15], so that the crystallinity of the CdS nanoparticles in the composite is kept.

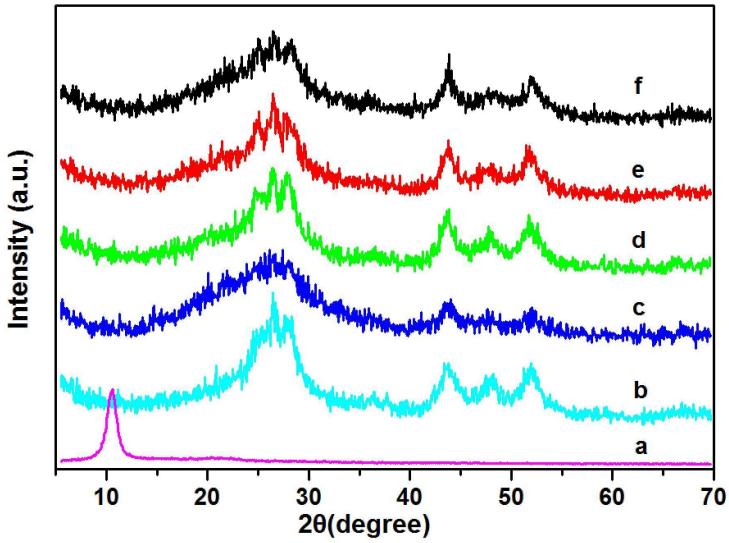

Fig. 1 XRD patterns of (a) GO, (b) CdS and (c-f) RGO /CdS-1%, 5%, 10%, 15% (weight ratios of RGO).

Furthermore, the morphology of the CdS and the RGO/CdS-10% samples was analyzed by SEM and TEM measurements, the results directly depict the morphology change of CdS in the presence of RGO sheets. Fig. 2a, b show a significant aggregation of CdS nanoparticles with an average diameter 200 ~ 400 nm in the absence of RGO. However, when GO was added during the microwave process, the morphology of the CdS became quite different. Fig. 2c shows a picture of the composite at low magnification. There are many small CdS nanospheres uniformly spread on the surface of the lamellar solid. As the magnification increases (Fig. 2d), it is clearly observed that the curled RGO sheets are tightly and evenly decorated by CdS nanospheres, indicating that strong interaction between RGO and CdS. The TEM and EDS results of the RGO/CdS-10% composites are displayed in Fig. 2e-f. Clearly, the RGO sheets are curled and corrugated and the CdS particles exhibit spherical morphology with less aggregation and a smaller diameter, which results in a larger specific surface area (see Table S1 in Supporting Information). It is obvious that the specific surface area of the nanocomposites is much larger than that of the pure CdS, and it increases with the increasing of the GO addition. The CdS spheres present a crumbly structure composed of smaller particles, which is beneficial for promoting its adsorbability as a photocatalyst[31]. At the same time, the EDS results in Fig. 2g reveal an elemental composition of C, Cd, S and Al (Al comes from the Al foil substrate), and the molar ratio of Cd to S is of nearly 1:1.

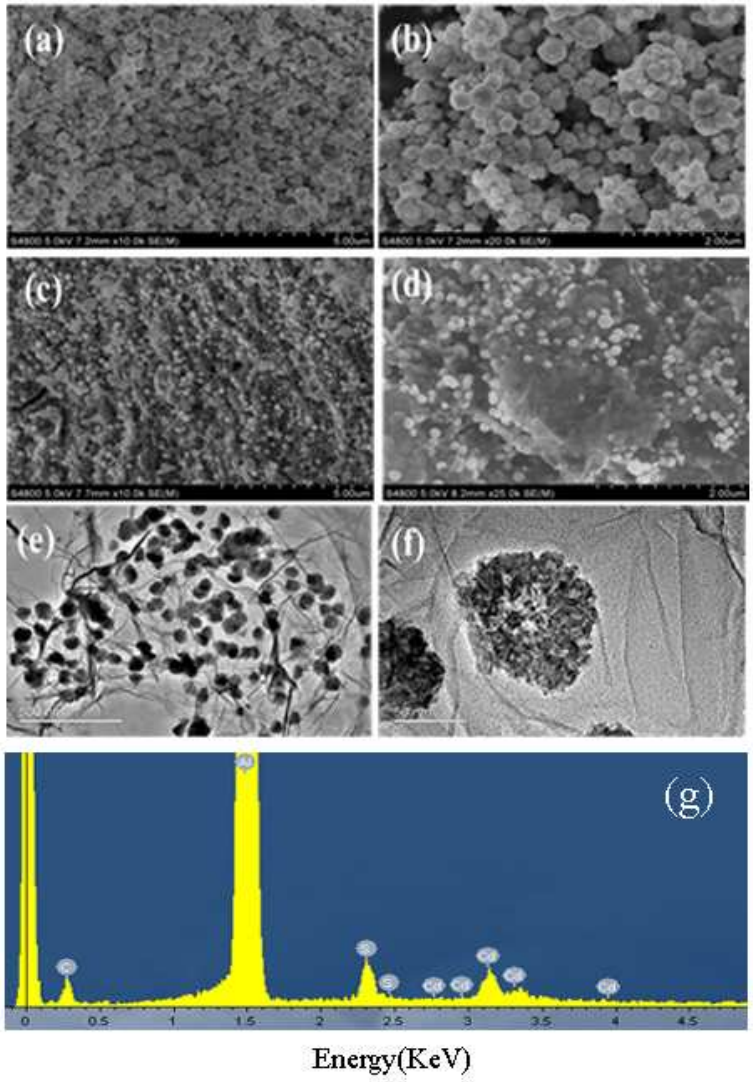

Fig. 2 SEM images of (a-b) CdS, and (c-d) SEM images, (e-f) TEM images, (g) EDS of the RGO/CdS-10% nanocomposite.

3.2 Chemical Composition of the RGO/CdS Nanocomposites

FTIR was used to measure the reduction degree of the GO sheets. The FTIR spectra of GO and the RGO/CdS samples over the range of 800-4000 cm^{-1} are shown in Fig. 3. In Fig. 3a, the characteristic GO bands are observed at 1042 cm^{-1} (C-O stretching vibrations of epoxy groups), 1224 cm^{-1} (C-O stretching vibrations of phenolic C-OH), 1402 cm^{-1} (O-H deformation

vibrations of tertiary C-OH) and 1734 cm^{-1} (C=O stretching vibrations of COOH groups). The peak at 1620 cm^{-1} is related to the H-O-H bending band of adsorbed H_2O molecules or to the skeletal vibrations of unoxidized C-C bonding[29, 32, 33]. All of these bands, which are related to the oxygen-containing functional groups almost vanished in the FTIR spectrum of the RGO/CdS composite as shown in Fig. 3b, thus indicating the reduction of GO. Simultaneously, the RGO/CdS composite shows a new peak around 1570 cm^{-1} due to the skeletal vibration absorption peak of the graphene sheets[34, 35]. In order to further demonstrate the reduction level of GO, the above results were verified by Raman and XPS data as follows.

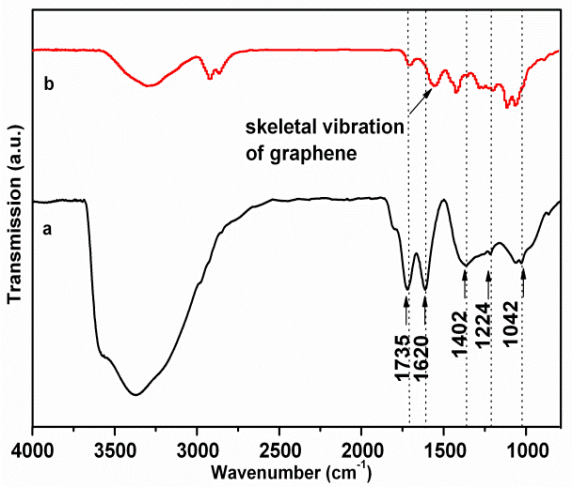

Fig. 3 FTIR spectra of (a) GO and (b) RGO/CdS-10%.

The Raman spectra also confirm the reduction of GO. As shown in Fig. 4b, there are two peaks around 294.8 cm^{-1} and 592 cm^{-1}, individually corresponding to the longitudinal optical photon mode (1-LO) and overtone (2-LO) of the CdS nanoparticles assembled on the RGO sheets[36]. Compared to the pure CdS, they slightly shift to the low frequency, which is caused by the small size effect. In addition, GO exhibits two prominent peaks at about 1369.4 cm^{-1} and 1593.6 cm^{-1} in Fig. 4c, which correspond to the D and G bands, respectively[37]. The RGO/CdS-10% sample also

contains both the D band (1364.9 cm^{-1}) and the G band (1584.6 cm^{-1}) which shift to the lower wavenumber due to the reduction of GO. Furthermore, compared with the pristine GO, a significant increase in the relative intensity of D/G is observed in the RGO/CdS-10% nanocomposite, which further proves the reduction of GO[38, 39].

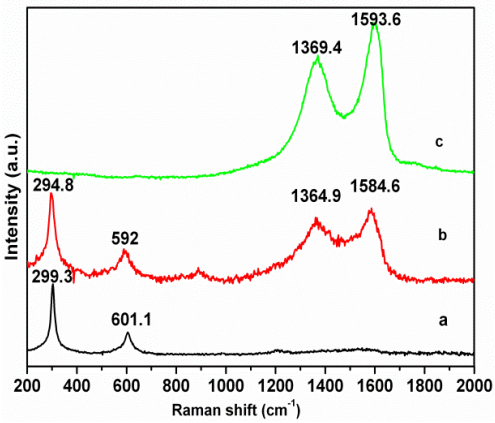

Fig. 4 Raman spectra of (a) CdS, (b) RGO/CdS-10% and (c) GO.

Other evidences come from the XPS spectra. The binding energies obtained in the XPS analysis are calibrated by referring to graphitic carbon at a binding energy of 284.7 eV. Fig. 5a and c show the full XPS spectra taken from the surface of GO and the RGO/CdS nanocomposites, respectively. As shown in Fig. 5b, four peaks located at 284.7 eV, 286.7 eV, 287.9 eV and 288.6 eV for the C1s deconvolution spectrum of GO correspond to C-C (sp^2 bonded carbon), C-OH (hydroxyls), C-O (carbonyls) and O-C=O (carboxyl), respectively. After microwave processing, as shown in Fig. 5d, only the C-C (sp^2 bonded carbon) peak is clearly observed at about 284.7 eV and the other peaks of the oxygenated groups are not detected, which means the GO was reduced. The calculated integral area ratio of O to C decreases from 1.36 for the GO to 1.16 for the RGO/CdS nanocomposites, which further proves the GO was partially reduced. In Fig. 5e-f, the peaks due to the Cd3d doublet are located at 404.4 eV and 411.1 eV, with a peak separation of 6.7 eV.

Similarly, the binding energy of the S2p peak is located at 161.5 eV. There are slight shifts in the Cd3d (from 405.5 eV to 404.4 eV, 412.2 eV to 411.1 eV) and S2p (from 165 eV to 161.5 eV) peaks to lower binding energies when compared to the standard values reported in the literature for CdS[40, 41]. The possible reason is that Cd atoms accept electrons from RGO, which causes the electron density around the Cd atoms to increase and thus for the Cd-S bond length to decrease[42]. Hence, the binding energies of Cd 3d and S 2p are reduced. The XPS data are consistent with the FTIR and Raman results, and all these outcomes further identify the reduction of GO and the formation of composites in the microwave process. It can be inferred that EG acts as a solvent as well as a reducing agent, resulting in the partial reduction of GO to RGO.

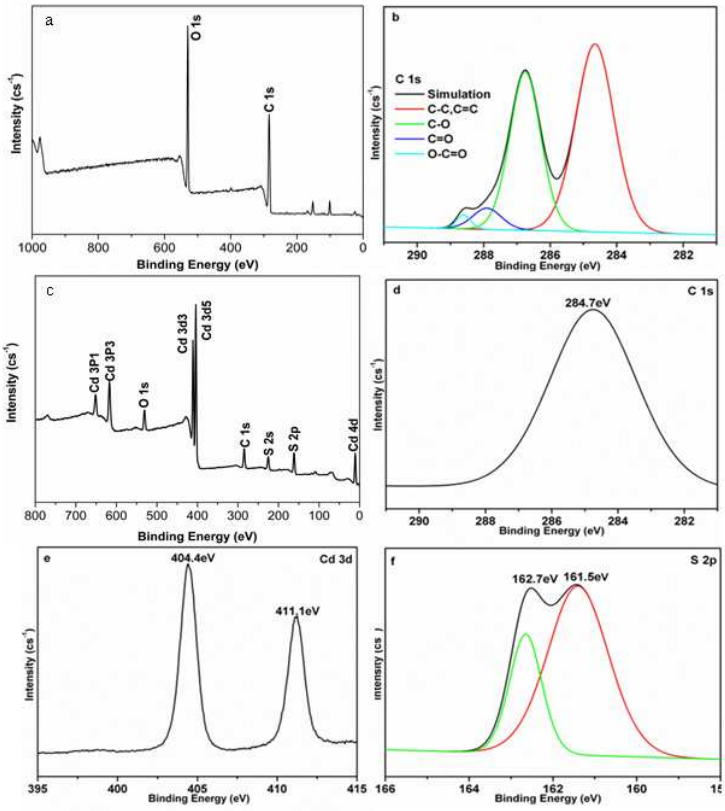

Fig. 5 XPS survey spectra of (a) GO and (b) peak deconvolution of C 1s, (c) XPS survey spectrum of RGO/CdS-10% and peak deconvolution of (d) C 1s, (e) Cd 3d, (f) S 2p.

3.3 Influence of RGO on the Properties of the RGO/CdS Nanocomposites

The comprehensive influence of RGO on the properties of the RGO/CdS nanocomposites has three major aspects: the increase in the response range to visible light, the improvement in electron-hole pair separation efficiency and the enhancement of the adsorbability for RhB molecules.

First of all, the adsorption range of light plays an important role in photocatalytic activity. On the macro level, the introduction of graphene deepens the color of the composites from lemon yellow to olive green, which indicates the absorption of visible light is enhanced. A comparison of the DRS spectra for a series of the RGO/CdS nanocomposites is shown in Fig. 6a. It is clear that RGO has a considerable influence on the absorbance of the samples in the visible-light region ($\lambda \geq 420$ nm). Compared with the pure CdS, the RGO/CdS nanocomposites exhibit a significantly enhanced absorbance with increasing the GO content that is consistent with the color change. In addition, the absorption edge of the RGO/CdS nanocomposites shows a gradual red shift compared with that of the pure CdS. As a result, the band gap of the RGO/CdS becomes narrower than the pure CdS as shown in Fig. 6b. A narrow band gap is an excellent property for a photocatalyst, because it results in a wider photoresponse range. The reduction of band gap can be ascribed to two reasons, one reason is the absorption contribution from RGO, and the other is the electrostatic binding or charge transfer interaction between CdS and the specific sites of carbon[43, 44].

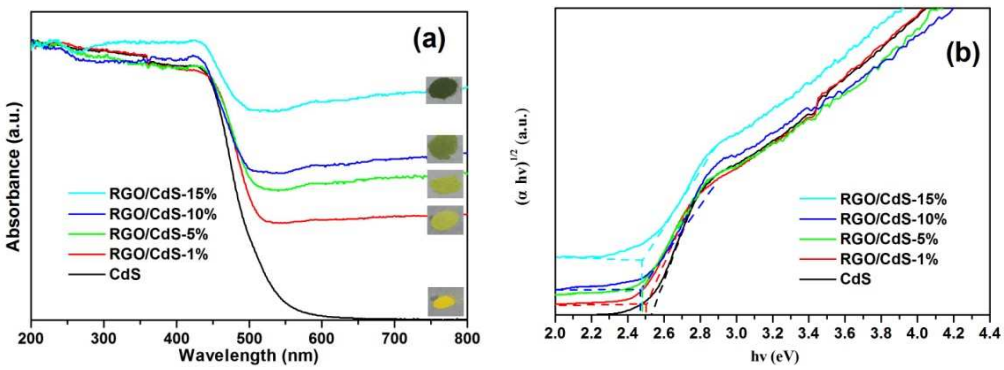

Fig. 6 (a) DRS and photos of series powder samples, and (b) band gap energies estimated by $(\alpha h\upsilon)^{1/2}$ versus the photo energy of the pure CdS and the RGO/CdS nanocomposites.

Secondly, it is widely accepted that the photocurrent is mainly determined by the electron-hole pair separation efficiency within the photoelectrodes[45]. Fig. 7a shows the photocurrent curves for the pure CdS and the RGO/CdS nanocomposites over several on-off cycles under intermittent visible light illumination. Apparently the photocurrent value returns back to almost the same value from zero as soon as the light is turned on, which suggests that the photocurrent behavior is reproducible. Notably, the RGO/CdS composites exhibit a much higher photocurrent value than the pure CdS. The improved photoresponse phenomenon can be attributed to the addition of RGO which serves as an excellent electron acceptor and mediator, prolonging the electron lifetime of the excited electrons and leading to minimal recombination of electron-hole pairs[16].

To further support the above proposition, electrochemical impedance spectroscopy (EIS) Nyquist plots were recorded for photo-electrodes consisting of the pure CdS and the RGO/CdS nanocomposites. In Fig. 7b, all samples show semicircles at high frequency which is related to the electrode resistance and also reflect the charge transfer resistance at the electrode/electrolyte solution interface. Clearly, the arc radii of the RGO/CdS samples decrease when compared with

the pure CdS, indicating that the RGO facilitates the interfacial charge transfer.

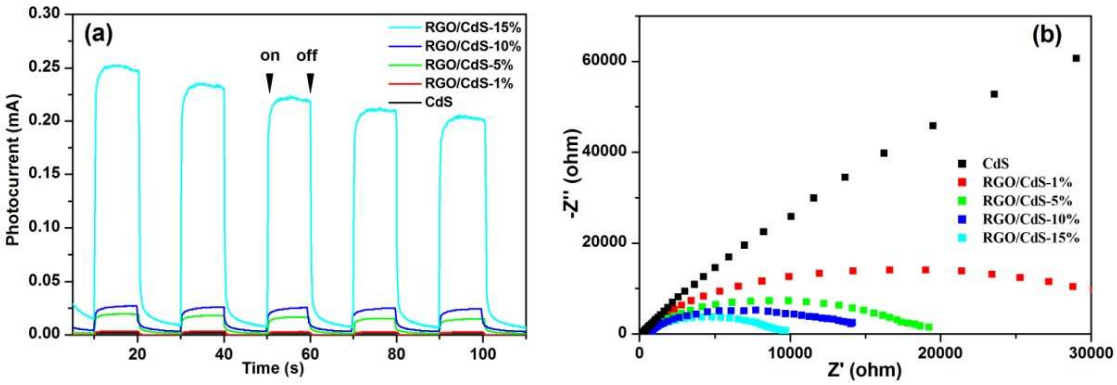

Fig. 7 (a) Transient photocurrent response and (b) Nyquist impedance plots of the pure CdS and the RGO/CdS nanocomposites with different RGO weight ratios.

Thirdly, another crucial factor for the photocatalytic process is the absorptive capacity of the photocatalyst. In comparison with the pure CdS, the RGO/CdS nanocomposites show better absorption ability due to its larger specific surface area. This improvement can be demonstrated by plotting the variation of absorbance after adsorption-desorption equilibrium (Figure S1, Supporting Information). Clearly, the adsorptive ability of the RGO/CdS is enhanced with increasing the GO content. When the GO content reaches a value of 10%, the adsorptive ability of the RGO/CdS reaches a maximum, which is consistent with the BET specific area data (Table S1, Supporting Information). The reason for the diversity in adsorptive activity is that a much higher content of RGO, such as 15%, limits the diffusion of the dye to the catalytical active site, shielding the incident light and thus reducing the photo-absorption of CdS.

3.4 Photocatalytic Activity of the RGO/CdS Nanocomposites

Fig. 8a shows a profile of the photocatalytic degradation efficiency of RhB for the pure CdS and the RGO/CdS nanocomposites under visible-light irradiation ($\lambda \geq 420$ nm). Clearly, there is little

decrease in the RhB concentration after irradiation in the absence of catalysts, which suggests that RhB is quite stable under visible light. It is also observed that the RGO/CdS nanocomposites (1%, 5%, 10% and 15%) exhibit better photocatalytic performance than the pure CdS, which implies that RGO can improve the photodegradation ability of CdS. Obviously, the optimum weight ratio is 10%, as this sample shows the highest photodegradation efficiency of 99.82% in 60 min. Too much RGO can shield the light from reaching the surface of the CdS photocatalysts. RGO may absorb some visible light and thus cause a light harvesting competition between CdS and RGO with the increase of the RGO content, which leads to the decrease of the photocatalytic performance. The excessive GR also can act as a kind of recombination center instead of providing an electron pathway and promote the recombination of electron–hole pairs in RGO.

From Fig. 8b, as the exposure time is extended, the intensity of the characteristic peak at 553 nm decreases dramatically and the absorption peaks become blue-shifted. After 60 min, the characteristic peak at 553 nm disappeared completely.

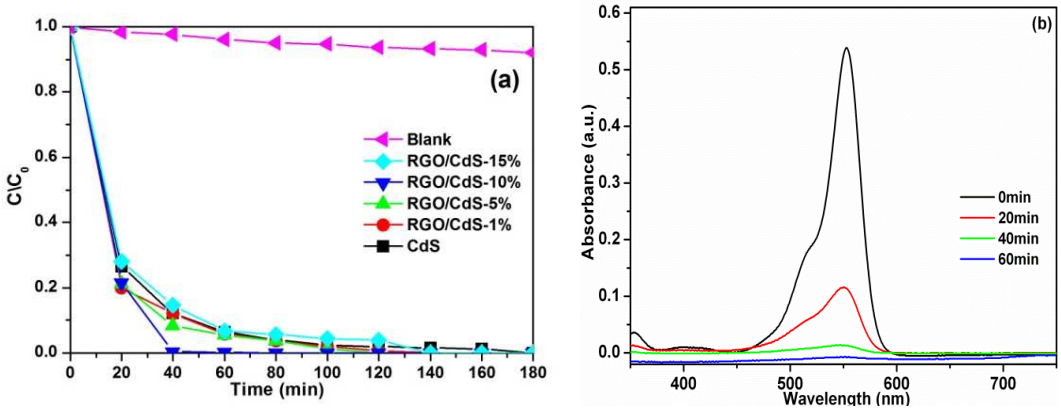

Fig. 8 (a) Variation of normalized C/C_0 concentration of RhB with irradiation time under visible light irradiation, and (b) time dependent UV-vis absorption spectrum of RhB in the presence of RGO/CdS-10%.

The stability of catalyst is a key factor for its practical applications. In order to characterize the stability of the pure CdS and the RGO/CdS-10% composites, a three-cycle photodegradation sequence for RhB (at the same initial concentration) was carried out with each cycle lasting for 80 min as shown in Fig. 9. There is no obvious deactivation for RGO/CdS-10% and the photodegradation efficiency after each run was 100%, 97.4% and 96%, while that for the pure CdS was 95.91%, 78.32% and 61.43%. The results imply that RGO can also enhance the stability of the nanocomposites in the photocatalytic role. The high electron conductivity of RGO can accept and shuttle photogenerated electrons from semiconductor CdS under visible light irradiation, which can effectively prevent CdS from photocorrosion and thus enhance the stability of CdS.

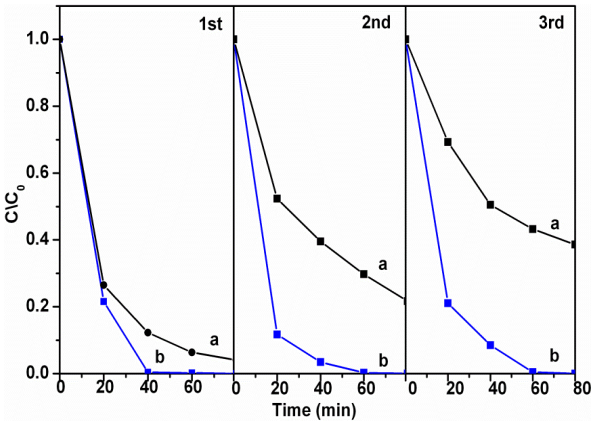

Fig. 9 Three-cycle photodegradation test of (a) CdS and (b) RGO/CdS-10% for RhB.

3.5 Tentative Mechanism of Photocatalytic Activity for the RGO/CdS Nanocomposites

According to our previously reported method[46], trapping experiments of hydroxyl radicals and holes were carried out to explore the main oxidants in the photodegradation process with the RGO/CdS-10% nanocomposites. Tert-butanol (TBA) and ethylenediaminetetraacetic acid disodium salt (EDTA-Na) were used as hydroxyl radical scavengers and holes scavengers, respectively. The photodegradation rates of RhB changes with the different addition amount of

TBA and EDTA-Na. These results indicate that both the radicals and the holes are the active oxidative species in the photodegradation of RhB with the RGO/CdS-10% nanocomposites.

On the basis of the above analysis, a schematic illustration of the possible process for photocatalytic degradation is shown in Fig. 10. Under visible light irradiation, charge separation in the CdS spheres is initiated and electron-hole pairs are generated. For the high carrier mobility in graphene, RGO can act as an electron acceptor and transporter to efficiently hinder the recombination of the photogenerated electron-hole pairs[6, 14]. The negative charge then activates dissolved oxygen to form the superoxide anion radical (O_2•$^-$)[15]. At the same time, the holes can react with the adsorbed water to produce the hydroxyl radical (•OH)[47]. Finally, the active species such as holes, superoxide anion radicals and hydroxyl radicals, all with strong oxidizing ability mineralize the RhB molecule to CO_2, H_2O or some other small molecule compound[48]. The proposed reaction chain is follows:

$CdS + h\nu \rightarrow CdS\ (e^- + h^+)$

$CdS\ (e^-) + RGO \rightarrow CdS + RGO\ (e^-)$

$e^- + O_2 \rightarrow O_2\bullet^-$

$OH^- + h^+ \rightarrow \bullet OH$

$RhB + O_2\bullet^- + \bullet OH + h^+ \rightarrow CO_2 + H_2O + \ldots$

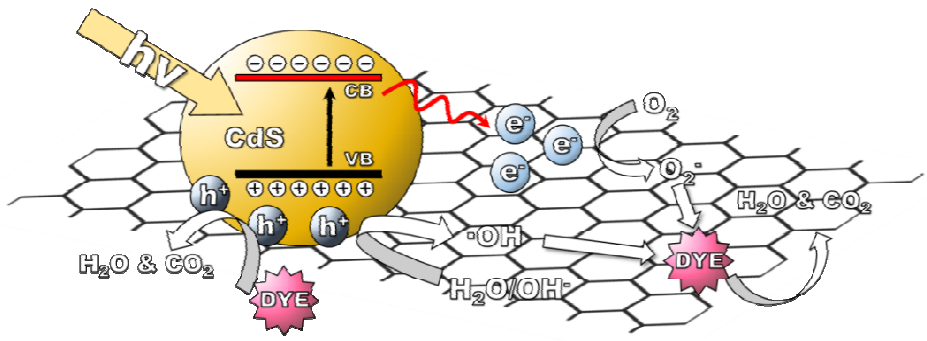

Fig. 10 Schematic illustration of the proposed mechanism for photodegradation process with the RGO/CdS nanocomposites under visible-light-irradiation.

4. Conclusions

In summary, a series of RGO/CdS nanocomposites with different GO weight ratios were synthesized via a microwave-assisted method, in which the room temperature ionic-liquid [BMIM]•SCN served both as the sulfur source and the stabilizing agent. The utilization of ionic-liquid simplified the fabrication procedure of the RGO/CdS nanocomposites. During the process, GO was partially reduced to RGO, which provided an important substrate for uniformed CdS nanoparticles to grow on. As compared to the pure CdS, the RGO/CdS nanocomposites possess excellent stability and improved photodegradation efficiency for the RhB solution under visible light irradiation. The improvement of the photocatalytic efficient for the CdS nanomaterials can be attributed to the existence of the RGO, which reinforces the adsorbability of the catalysts, extends the light absorption range and suppresses the electron-hole pair recombination, simultaneously. These findings may present new possibilities for the design and controlling synthesis of visible-light-sensitive, stable and efficient photocatalytic nanocomposites.

Supporting Information

BET specific area of CdS and RGO/CdS (Table S1) and the variation of absorbance after adsorption-desorption equilibrium for CdS and RGO/CdS with different RGO weight ratios （Figure S1）.

AUTHOR INFORMATION

Corresponding Authors

*E-mail: wuyz@sdu.edu.cn; zhengxie@mail.ipc.ac.cn

Notes

The authors declare no competing financial interest.

Acknowledgements

This work was supported by National Basic Research Program of China (2011CB301904), NSFC (Contract No. 51321091), IIFSDU and the Fundamental Research Funds of Shandong University.

References

1. Xiang Q., Yu J., Graphene-based Photocatalysts for Hydrogen Generation, *J. Phys. Chem. Lett.* **2013**, 4, 753−759.

2. Bao, N.; Shen, L.; Takata, T.; Domen, K. Self-Templated Synthesis of NanoporousCdS Nanostructures for Highly Efficient Photocatalytic Hydrogen Production under Visible Light. *Chem. Mater*. **2007**, *20*, 110-117.

3. Li, Y.; Ma, G.; Peng, S.; Lu, G.; Li, S. Photocatalytic H_2Evolution over Basic Zincoxysulfide ($ZnS_{1-x-0.5y}O_x(OH)_y$) under Visible Light Irradiation. *Appl. Catal. A: Gen.* **2009**, *363*, 180-187.

4. Reber, J. F.; Rusek, M. Photochemical Hydrogen Production with Platinized Suspensions of Cadmium Sulfide and Cadmium Zinc Sulfide Modified by Silver Sulfide. *J. Phys. Chem.* **1986**, *90*, 824-834.

5. Sheeney-Haj-Ichia, L.; Basnar, B.; Willner, I. Efficient Generation of Photocurrents by Using CdS/Carbon Nanotube Assemblies on Electrodes. *Angew. Chem. Int. Ed.* **2005**, *44*, 78-83.

6. Li, Q.; Guo, B.; Yu, J.; Ran, J.; Zhang, B.; Yan, H.; Gong, J. R. Highly Efficient Visible-Light-driven Photocatalytic Hydrogen Production of CdS-cluster-decorated Graphene Nanosheets. *J. Am. Chem. Soc.* **2011**, *133*, 10878-10884.

7. Chen, Y.; Rosenzweig, Z. Luminescent CdS Quantum Dots as Selective Ion Probes. *Anal. Chem.* **2002**, *74*, 5132-5138.

8. Entezari, M. H.; Ghows, N. Micro-emulsion under Ultrasound Facilitates the Fast Synthesis of Quantum Dots of CdS at Low Temperature. *Ultrason. Sonochem.* **2011**, *18*, 127-134.

9. Chen, W.-T.; Yang, T.-T.; Hsu, Y.-J. Au-CdS Core−shell Nanocrystals with Controllable Shell Thickness and Photoinduced Charge Separation Property.*Chem. Mater.* **2008**, *20*, 7204-7206.

10. Sheeney-Haj-Ichia, L.; Pogorelova, S.; Gofer, Y.; Willner, I. Enhanced Photoelectrochemistry in CdS/Au Nanoparticle Bilayers. *Adv. Funct. Mater.* **2004**, *14*, 416-424.

11. Baker, D. R.; Kamat, P. V. Photosensitization of TiO_2 Nanostructures with CdS Quantum Dots: Particulate versus Tubular Support Architectures. *Adv. Funct. Mater.***2009**, *19*, 805-811.

12. Hu, Y.; Liu, Y.; Qian, H.; Li, Z.; Chen, J. Coating Colloidal Carbon Spheres with CdS Nanoparticles: Microwave-assisted Synthesis and Enhanced Photocatalytic Activity. *Langmuir* **2010**, *26*, 18570-18575.

13. Shi, Y.; Li, H.; Wang, L.; Shen, W.; Chen, H. Novel α-Fe_2O_3/CdSCornlikeNanorods with Enhanced Photocatalytic Performance. *ACS Appl. Mater. Interfaces.***2012**, *4*, 4800-4806.

14. Liu, X.; Pan, L.; Lv, T.; Zhu, G.; Sun, Z.; Sun, C. Microwave-assisted Synthesis of CdS-reduced Graphene Oxide Composites for Photocatalytic Reduction of Cr(VI). *Chem. Comm.***2011**, *47*, 11984-11986.

15. Zhang, N.; Zhang, Y.; Pan, X.; Fu, X.; Liu, S.; Xu, Y. J. Assembly of CdS Nanoparticles on the Two-dimensional Graphene Scaffold as Visible-light-driven Photocatalyst for Selective Organic Transformation under Ambient Conditions. *J. Phys. Chem. C* **2011**, *115*, 23501-23511.

16. Chen, Z.; Liu, S.; Yang, M.-Q.; Xu, Y.-J. Synthesis of Uniform CdS Nanospheres/Graphene Hybrid Nanocomposites and Their Application as Visible Light Photocatalyst for Selective

Reduction of Nitro Organics in Water. *ACS Appl. Mater. Interfaces*.**2013**, *5*, 4309-4319.

17. Antonietti, M.; Kuang, D.; Smarsly, B.; Zhou, Y. Ionic Liquids for the Convenient Synthesis of Functional Nanoparticles and Other Inorganic Nanostructures. *Angew. Chem. Int. Ed.* **2004**, *43*, 4988-4992.

18. Ma, J.; Liu, X.; Lian, J.; Duan, X.; Zheng, W. Ionothermal Synthesis of BiOCl Nanostructures via a Long-chain Ionic Liquid Precursor Route. *Cryst. Eng. Comm.* **2010**, *10*, 2522-2527.

19. Zhu, H.; Huang, J.-F.; Pan, Z.; Dai, S. Ionothermal Synthesis of Hierarchical ZnO Nanostructures from Ionic-liquid Precursors. *Chem. Mater.* **2006**, *18*, 4473-4477.

20. Kaper, H.; Willinger, M.-G.; Djerdj, I.; Gross, S.; Antonietti, M.; Smarsly, B. M. IL-assisted Synthesis of V_2O_5 Nanocomposites and VO_2 Nanosheets. *J. Mater. Chem.* **2008**, *18*, 5761-5769.

21. Lou, Z.; Huang, B.; Qin, X.; Zhang, X.; Wang, Z.; Zheng, Z.; Cheng, H.; Wang, P.; Dai, Y. One-step Synthesis of AgBr Microcrystals with Different Morphologies by ILs-assisted Hydrothermal Method. *Cryst. Eng. Comm.* **2011**, *13*, 1789-1793.

22. Wu, Y.; Hao, X.; Yang, J.; Tian, F.; Jiang, M. Ultrasound-assisted Synthesis of Nanocrystalline ZnS in the Ionic Liquid [BMIM]•BF_4. *Mater.Lett.* **2006**, *60*, 2764-2766.

23. Bowers, J.; Butts, C. P.; Martin, P. J.; Vergara-Gutierrez, M. C.; Heenan, R. K. Aggregation Behavior of Aqueous Solutions of Ionic Liquids. *Langmuir* **2004**, *20*, 2191-2198.

24. Jana, M. K.; Biswas, K.; Rao, C. N. R. Ionothermal Synthesis of Few-layer Nanostructures of Bi_2Se_3 and Related Materials. *Chem-Eur J.* **2013**, *19*, 9110-9113.

25. Ma, J.; Lei, D.; Mei, L.; Duan, X.; Li, Q.; Wang, T.; Zheng, W. Plate-like SnS_2Nanostructures: Hydrothermal Preparation, Growth Mechanism and Excellent Electrochemical Properties. *Cryst. Eng. Comm.* **2012**, *14*, 832-836.

26. Biswas, K.; Rao, C. N. R. Use of Ionic Liquids in the Synthesis of Nanocrystals and Nanorods of Semiconducting Metal Chalcogenides. *Chem-Eur J.* **2007**, *13*, 6123-6129.

27. Behboudnia, M.; Habibi-Yangjeh, A.; Jafari-Tarzanag, Y.; Khodayari, A. Preparation and Characterization of Monodispersed Nanocrystalline ZnS in Water-rich [EMIM]$EtSO_4$ Ionic Liquid Using Ultrasonic Irradiation. *J. Cryst. Growth* **2008**, *310*, 4544-4548.

28. Dreyer, D. R.; Park, S.; Bielawski, C. W.; Ruoff, R. S. The Chemistry of GrapheneOxide. *Chem. Soc. Rev.* **2010**, *39*, 228-240.

29. Nakajima, T.; Mabuchi, A.; Hagiwara, R. A New Structure Model of Graphite Oxide. *Carbon***1988**, *26*, 357-361.

30. Pan, D.; Wang, S.; Zhao, B.; Wu, M.; Zhang, H.; Wang, Y.; Jiao, Z. Li Storage Properties of Disordered Graphene Nanosheets. *Chem. Mater.* **2009**, *21*, 3136-3142.

31. Luo, M.; Liu, Y.; Hu, J.; Liu, H.; Li, J. One-Pot Synthesis of CdS and Ni-Doped CdS Hollow Spheres with Enhanced Photocatalytic Activity and Durability. *ACS Appl. Mater. Interfaces.* **2012**, *4*, 1813-1821.

32. Szabó, T.; Tombácz, E.; Illés, E.; Dékány, I. Enhanced Acidity and pH-dependent Surface Charge Characterization of Successively Oxidized Graphite Oxides. *Carbon* **2006**, *44*, 537-545.

33. Guo, H.-L.; Wang, X.-F.; Qian, Q.-Y.; Wang, F.-B.; Xia, X.-H. A Green Approach to the Synthesis of Graphene Nanosheets. *ACS Nano* **2009**, *3*, 2653-2659.

34. Nethravathi, C.; Rajamathi, M. Chemically Modified Graphene Sheets Produced by the Solvothermal Reduction of Colloidal Dispersions of Graphite Oxide. *Carbon* **2008**, *46*, 1994-1998.

35. Bourlinos, A. B.; Gournis, D.; Petridis, D.; Szabó, T.; Szeri, A.; Dékány, I. Graphite Oxide: Chemical Reduction to Graphite and Surface Modification with Primary Aliphatic Amines and Amino Acids. *Langmuir* **2003**, 19, 6050-6055.

36. Arguello, C. A.; Rousseau, D. L.; Porto, S. P. S. First-Order Raman Effect in Wurtzite-type Crystals. *Phys. Rev.***1969**, *181*, 1351-1363.

37. He, H.; Riedl, T.; Lerf, A.; Klinowski, J. Solid-state NMR Studies of the Structure of Graphite Oxide. *J. Phys. Chem.* **1996**, *100*, 19954-19958.

38. Stankovich, S.; Dikin, D. A.; Piner, R. D.; Kohlhaas, K. A.; Kleinhammes, A.; Jia, Y.; Wu, Y.; Nguyen, S. T.; Ruoff, R. S. Synthesis of Graphene-based Nanosheets via Chemical Reduction of Exfoliated Graphite Oxide. *Carbon* **2007**, *45*, 1558-1565.

39. Chen, S.; Zhu, J.; Wang, X. One-Step Synthesis of Graphene−Cobalt Hydroxide Nanocomposites and Their Electrochemical Properties. *J. Phys. Chem. C* **2010**, *114*, 11829-11834.

40. Vemuri, R. S.; Gullapalli, S. K.; Zubia, D.; McClure, J. C.; Ramana, C. V. Structural and Chemical Properties of Highly Oriented Cadmium Sulfide (CdS) Cauliflower Films. *Chem. Phys. Lett.* **2010**, *495*, 232-235.

41. Pan, S.; Liu, X. CdS-Graphene Nanocomposite: Synthesis, Adsorption Kinetics and High Photocatalytic Performance under Visible Light Irradiation. *New J. Chem.***2012**, *36*, 1781-1787.

42. Nair, M. T. S.; Nair, P. K.; Zingaro, R. A.; Meyers, E. A. Conversion of Chemically Deposited Photosensitive CdS Thin Films to n-type by Air Annealing and Ion Exchange Reaction. *J. Appl. Phys.***1994**, *75*, 1557-1564.

43. Zhang, Y.; Tang, Z.-R.; Fu, X.; Xu, Y.-J. TiO_2−graphene Nanocomposites for Gas-phase Photocatalytic Degradation of Volatile Aromatic Pollutant: Is TiO_2−graphene Truly Different from Other TiO_2−carbon Composite Materials? *ACS Nano***2010**, *4*, 7303-7314.

44. Sakthivel, S.; Kisch, H. Daylight Photocatalysis by Carbon-modified Titanium Dioxide. *Angew. Chem. Int. Ed.* **2003**, *42*, 4908-4911.

45. Ye, H.; Park, H. S.; Bard, A. J. Screening of Electrocatalysts for Photoelectrochemical Water Oxidation on W-Doped $BiVO_4$ Photocatalysts by Scanning Electrochemical Microscopy. *J. Phys. Chem. C* **2011**, *115*, 12464-12470.

46. Xiu, Z.; Bo, H.; Wu, Y.; Hao X. Graphite-like C_3N_4 modified Ag_3PO_4 nanoparticles with highly enhanced photocatalytic activities under visible light irradiation. *Applied Surface Science* **2014**, *289*, 394-399.

47. Khan, Z.; Chetia, T. R.; Vardhaman, A. K.; Barpuzary, D.; Sastri, C. V.; Qureshi, M. Visible Light Assisted Photocatalytic Hydrogen Generation and Organic Dye Degradation by CdS-metal Oxide Hybrids in Presence of Graphene Oxide. *RSC Adv.* **2012**, *2*, 12122-12128.

48. Martínez-de la Cruz, A.; Marcos Villarreal, S.M.G.; Torres-Martínez, L.M.; López Cuéllar, E.; Ortiz Méndez, U.; Photoassisted degradation of rhodamine B by nanoparticles of α-$Bi_2Mo_3O_{12}$ prepared by an amorphous complex precursor, *Mater. Chem. Phys.*, **2008**, *112*, 679-685.